Dimensionless Analysis of the Transition from Continuous Jet Mode to Natural Pulsation in Electrohydrodynamic Jet Printing

Ali Bahrami[1], Angelo Hawa[1], Kaifan Yue[2], Kira Barton[1,2]

***Abstract*— Electrohydrodynamic jet (e-jet) printing is a promising additive manufacturing technique that has demonstrated high-resolution fabrication capabilities. Various jetting regimes as a function of the input voltage signal have been identified and studied. In DC printing, a transition has been observed from the continuous jet to the natural pulsation mode, which precipitates less predictable outcomes on the print rate and quality of the final pattern. This phenomenon is not well understood, and its behavior is yet to be characterized. Accordingly, the natural pulsation initiation (NPI) of 15 solutions with unique viscosities and conductivities was analyzed. Dimensionless parameters referencing material properties (Ohnesorge and ratio of capillary to charge relaxation time), applied voltage (electric capillary), and induced flow rate (Weber) are implemented to analyze the dynamics of this transition. Our findings indicate that NPI is generally more prevalent in inks with higher conductivities. Additionally, less viscous inks appeared to inhibit NPI, providing a larger design space for attaining stable behavior.**

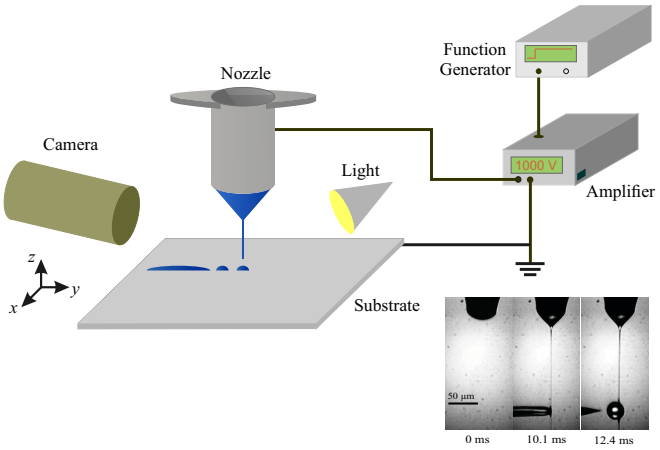

Fig. 1: Schematic figure of a sample electrohydrodynamic (e-jet) printing process.

I. INTRODUCTION

Electrohydrodynamic jet (e-jet) printing is an auspicious micro-additive manufacturing technique that involves the precise deposition of submicroliter liquid droplets from a nozzle aperture. With demonstrated applications in printed electronics [1, 2], biosensors [3, 4], and optical devices [5], the high-resolution capabilities of e-jet printing provide a clear pathway for its continued research and development. In contrast with traditional inkjet printing techniques that utilize piezoelectric or thermal actuation, the e-jet printing mechanism is electrically driven from the nozzle exterior. This distinction has been shown to fabricate patterned features of significantly higher resolution.

In e-jet printing, a localized electric potential is applied between the nozzle and the substrate, which induces a flow of mobile ions towards the ink meniscus. The resulting charge accumulation deforms the spherical meniscus to a conical shape, known as a *Taylor cone*. As the applied potential increases, the downward electric force overcomes the opposing capillary and surface tension forces, causing a jet of ink to expel from the nozzle aperture. Fig. 1 provides a schematic of an e-jet printing setup. For liquids with a relatively high viscosity, a syringe pump or back pressure is often coupled with the nozzle to augment the downward stress. However, this practice can lead to lower quality prints in less viscous inks due to excessive ink withdrawal.

The applied voltage can take the form of a constant or modulated signal. The former is known as DC printing, while the latter results in either pulsed or drop-on-demand (DoD) printing [3, 6, 7]. Following the voltage application, the deformation of the spherical meniscus to a conical shape is known as the cone-jet regime. A variety of jetting modes within this regime have been characterized as a function of the supplied voltage and flow rate inputs. One example is the *continuous-jet* mode, which is most favorable for DC printing. This printing mode is distinguished by the sustained formation of a contiguous jet of ink from the nozzle to the substrate, resulting in a relatively consistent flow rate delivery. While only pertinent in certain applications, applying a constant DC voltage is preferred when studying the general behavior of the different jetting regimes.

Pulsating jet is another mode of the cone-jet regime that is characterized by the periodic ejection of an ink droplet. This regime can either be triggered naturally by applying a constant DC voltage (natural pulsation) or triggered extrinsically by applying a modulated voltage, e.g. pulsed DC voltage [8]. *Pulsating jet* mode induced by a pulsed DC signal is widely employed in the manufacturing industry to produce high-resolution, and continuous patterns. Printing with pulsed DC voltage is found to have the advantage of higher efficiency and spacial resolution than constant DC voltage-induced printing because it enables precise control over droplet size and spacing through properly tuned pulse width and frequency [7]. Modulating and superimposing pulsed signals with varying frequencies and pulse widths

[1] Mechanical Engineering Department, University of Michigan, 2350 Hayward St., Ann Arbor, MI 48109, USA bahrami@umich.edu
[2] Department of Robotics, University of Michigan, 2505 Hayward St., Ann Arbor, MI 48109, USA bartonkl@umich.edu

enable DoD functionality of e-jet. With both spatial and temporal control of printed materials, DoD is used to fabricate a variety of functional devices including high-resolution conductive interconnects [9] and electrochemical sensors [3].

A transitional behavior between these two cone-jet regimes known as *Natural Pulsation Initiation* (NPI) is reported in our previous publication [10] for a setup with no supplied flow rate. This transition is characterized by the brief presence of a continuous jet preceding naturally pulsating ejections. This phenomenon can occur at an array of applied voltages with no process or parameter changes. NPI can be categorized as a system instability, and its unintentional instigation can have negative consequences on printing rate, controllability, and quality. Though initially observed under the effect of a constant DC voltage, NPI can also be present during pulsed jetting at sufficiently long pulse widths. Consequently, a thorough investigation of the prevalence and preventability of NPI is needed to identify the impact of various system inputs to determine their influence on this phenomenon. Fig. 2 displays a sequence of labelled images depicting the progression of NPI.

Various aspects of natural pulsation have been widely studied. Juraschek and Röllgen [11] first identified natural pulsating phenomenon as a result of imbalance between the ejection rate of the liquid and its supply rate. And they further studied the effect of supplied flow rate, charge concentration, and surface tension on pulsation frequency. Collins et al [12] theorized scaling laws for ejected droplet radius and charge, and identified three scaling regimes based on conductivity of the liquid. Chen et al [13] further derived analytical models for the dependency of pulsation frequency and ejection volume on the applied voltage. Choi et al [14] experimentally studied the natural pulsation mode and discovered relation between nozzle size and jet diameter, and verified scaling laws between pulsation frequency and applied voltage. Guo et al [15] took a statistical approach by performing regression analysis on experimental data and proposed a model relating material properties like viscosity and conductivity to ejection volume. Hijano et al [16] investigated pulsation frequency and droplet diameter using dimensionless parameters representing flow rate and electric Bond number.

However, no studies have analyzed the aggravating factors for the NPI phenomenon across a multitude of material properties and applied voltages. Utilizing dimensionless representatives for these system inputs provides a more generally applicable analysis and reduces the experimental workload for future studies. This paper analyzes the prevalence and characteristics of NPI across 15 liquids with varying viscosities and conductivities. Dimensionless parameters are used to refer to these particular material properties, in addition to the applied voltage and flow rate. The main contributions of this work are (1) Understanding the root cause of the NPI phenomenon and (2) Determining the effect of ink conductivity and viscosity on the characteristics of NPI. The rest of the paper is organized as follows: Section II provides descriptions of the experimental setup and methods, Section III outlines the experimental results, Section IV contains concluding arguments and details future work, and the Appendices provide additional procedural details and validation.

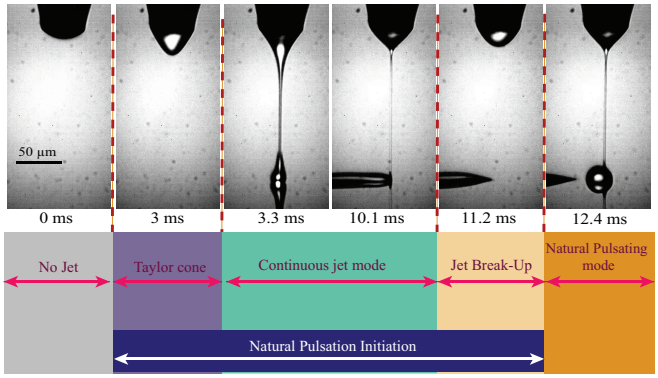

Fig. 2: Sequence of images depicting phases of Natural Pulsation Initiation (NPI) in DC electrohydrodynamic jet (e-jet) printing.

II. Methods and Procedure

A. Experimental Setup

A custom-built e-jet printer developed by the Barton Research Group was used to conduct all experiments. The setup consists of a four-axis motion system, a print head, and high-speed imaging equipment. For the motion system, precise positioning of the substrate is achieved through the integration of a single-axis lift stage (Aerotech, ANT130) with a two-axis linear stage (Aerotech, Planar$_{DL}$). Mounted directly above the substrate is a 3D-printed syringe holder containing electrical connections. The motion of the syringe and micronozzle was controlled with a nanopositioning lift stage (Aerotech, BMS60). A high-speed camera (Vision Research, Phantom VEO-410L) and a coaxial LED light (Advanced Illumination, SL162) are located adjacent to the motion system. The substrate is a silicon wafer with a resistivity of $0.005 - 0.02$ Ω-cm and rests suctioned to an electrically grounded aluminum disc. To ensure good conductivity, gold sputter coating was performed on 15 glass nozzles containing an average inner diameter of 35.95 μm and standard deviation of 0.92 μm. A voltage amplifier (TREK, 677B) and a function generator (RIGOL, DG1032Z) serve as the input trigger for the high-speed camera and supply a high electric potential to the nozzle using mini hook test leads. The nozzle aperture was positioned at 150 μm above the silicon substrate. The high-speed camera settings were configured to capture 10 000 frames per second with an exposure time of 80 μs. The dimension of each frame is 1024×512 pixels with a resolution of 4.55 px/μm.

B. Dimensionless Parameters

Various theoretical models, such as the leaky-dielectric model by Melcher & Taylor, provide analytical relationships that describe electrohydrodynamic (EHD) processes [17, 18]. Manipulating EHD equations in their dimensionless form generalizes fluid flow dynamics [19]. Hence, using scales

for characteristic quantities of e-jet printing provides four main dimensionless numbers. This article implements the nondimensionalization techniques of [19]. Two significant characteristic time constants in e-jet printing are the capillary time, $t_\gamma = \sqrt{\rho_i R^3/\gamma}$, and charge relaxation time, $t_e = \varepsilon_r \varepsilon_0 / K_i$. γ is the surface tension, R is the radius of the nozzle aperture, and ρ_i is the ink's density. K_i is the conductivity and ε_r is the relative permittivity of the ink, while ε_0 is the permittivity of free space ($\varepsilon_0 = 8.854 \times 10^{-12} F/m$). By using these characteristic times and other scalar parameters, the following four main dimensionless numbers can be calculated: (1) Ohnesorge number, relating the viscous forces to inertial and surface tension forces $Oh = \mu_i / \sqrt{\rho_i \gamma R}$, where μ_i is the viscosity of the ink; (2) relaxation parameter, the ratio of capillary to charge relaxation times, $\alpha = t_\gamma / t_e = \left[\rho_i R^3 {K_i}^2 / (\varepsilon_r^2 \varepsilon_0^2 \gamma)\right]^{1/2}$; (3) Weber number, the ratio of inertia to capillary forces, $We = \rho_i U^2 R / \gamma$, where U is the average inlet velocity, and (4) electric capillary number, comparing the electric force to the capillary force, $Ca_E = \varepsilon_0 E^2 R / \gamma$. E is the electric field strength and its relationship to electric potential is $E = V / [R \ln(2H/R)]$, where H is the standoff height between the nozzle and grounded substrate. More details about the governing equations and nondimensionalization of EHD equations can be found in [19].

C. Experimental Procedure

Prior to experimentation, each nozzle was initialized to promote stability by applying voltages ranging from 1000 V to 1200 V for several minutes. A lower bound for the experimental voltages was found by incrementally increasing the applied voltage until initial jet formation.

Preceding the high voltage application, the x-y stage was set to translate linearly at a velocity of $V_s = 20$ mm/s $\pm 0.015\%$ for a distance of 25 mm. The high-speed camera was triggered to record at the onset of the voltage pulse, which had a duration of 741 ms. For each trial, the voltage was incrementally increased until either the observation of a fully continuous jet or the occurrence of nozzle arcing, which is an unsteady jetting disturbance leading to nozzle failure.

D. Ink Preparation

Fifteen liquids of varying properties were prepared by combining precise amounts of glycerine, deionized (DI) water, and a solution of 0.5 g NaCl in 80 mL DI water. Each liquid contained a unique viscosity (μ) and conductivity (K) from the set $\mu \in \{40,60,80\}$ mPa·s and K $\in \{2,4,6,8,10\}$ μ S/cm. Additional properties, including density, surface tension, and relative permittivity were approximately constant. The solution recipe for each liquid was gathered from Guo et al [15]. The average contact angle of the liquid was measured to be $45 \pm 0.5\%$. A table detailing the compositions and properties of the experimental inks is provided in Appendix III.

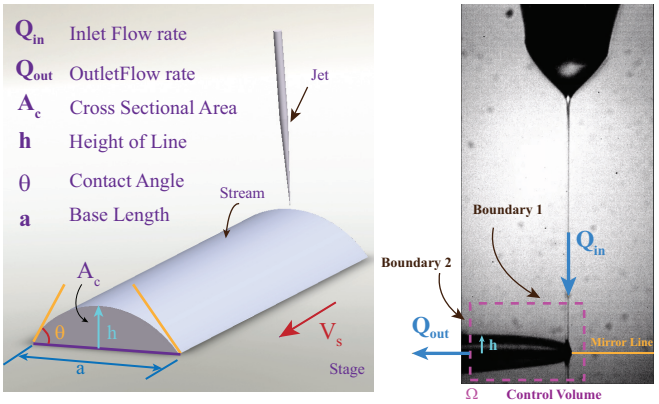

Fig. 3: Schematic figure of the control volume concept and cross-sectional area of the printed line.

E. Flowrate Approximation

Due to the lack of flow rate monitoring equipment, a system modeling technique was incorporated for approximating the Weber number of the continuous ink stream as a function of time. These measurements were obtained by applying a control volume concept to the series of captured frames, as shown in Fig. 3. The continuity equation ensures that for steady flow, the flow rates entering and exiting the control volume are equivalent. This relationship is provided in Eq. (1).

$$\dot{V} = \int_\Omega u \mathrm{d}\Omega = Q_{in} - Q_{out} = 0 \Rightarrow Q_{in} = Q_{out} \quad (1)$$

where $\dot{V}$ is the rate of volumetric change, u is the velocity of the liquid and Ω is the boundary of the control volume. Q_{in} is the entering volumetric flow rate to the control volume and Q_{out} is the exiting volumetric flow rate. [20]

Assuming an underdeveloped boundary layer at the control volume outlet (Boundary 2 in Fig. 3), the velocity of the liquid is equal to the preset stage velocity. Hence, the exiting flow rate is represented as $Q_{out} = V_s \times A_c$, where A_c is the cross-sectional area of the printed line at boundary number 2. Due to the cohesive nature of the inks, A_c cannot be directly measured. Therefore, a method for approximating A_c is developed based on two main assumptions as follows:

ASSUMPTION 1: *The continuous line of ink expresses identical spreading behavior to a sessile droplet.* After depositing any volume of liquid, it will wet the surface until the liquid and substrate reach an equilibrium state and the interfacial energies balance one another. The contact angle is characteristic of this equilibrium [21, 22]. This assumption states that the contact angle and dimensional proportions (thickness to height ratio) between a uniform continuous stream and a printed droplet are identical [21, 22].

ASSUMPTION 2: *The dimensional proportions (ratio of height to the base of a droplet) are volume independent for each liquid.* This statement assumes that the printed droplets are sufficiently small as to not be deformed by gravitational forces [21]. The proportionality constant was measured for

each liquid to validate this assumption. Fig. 9 in Appendix II provides empirical measurements of this ratio for four different liquids.

The conclusion from these assumptions reveals that the cross-sectional areas (A_c) of a droplet and printed line of the same height are identical. Similar image processing techniques as in [10] were implemented to obtain an estimate of the height (h). Then, using the proportionality ratio (h/a) to find the base diameter (a), the cross-sectional area can be calculated by a circular cap model as shown in Eq. (2).

$$R = \frac{a^2 + 4h^2}{8h}$$
$$A_c = R^2 cos^{-1}(\frac{R-h}{h}) - (R-h)\sqrt{2Rh - h^2} \quad (2)$$

where a is the chord length, R is the radius of circle, and h is the height of the sector [23].

In summary, this model provides a relationship mapping the height of the continuous line to the Weber number of the flow. Further details are provided in Appendix I.

F. Model Validation

Validation for the method described in section II-E was performed by analyzing the videos that demonstrated a clear spatial separation between the continuous stream deposited during NPI and the subsequent pulsating ejections. Due to the cohesive nature of the liquids, the linear NPI deposition coalesced into one or more oblate spheroidal droplets several seconds after impingement. An ellipsoidal cap model was utilized to estimate the volume of this initial deposition, and its corresponding height and axes lengths were measured with a digital microscope (Dino-Lite, AM73515MT8A). Eq. (3) provides a formula for calculating the volume of a ellipsoidal cap model.

$$V = \frac{\pi}{6(1-e^2)}(3(1-e^2)R^2 + h^2)h \quad (3)$$

where e is the eccentricity of the ellipse, R is the semi-major axis, and h is the height of the droplet.

Considering the ellipsoidal model as the expected value, the percent error of the flow rate model was calculated and is presented for various trials in Table I. A significant portion of the error can be attributed to initial transient behavior in the jet's flow rate. This behavior is expanded on in Section III.

Case#	I	II	III	IV	V	Average
Error [%]	11.76	12.75	15.85	10.33	2.70	10.68

TABLE I: The percentage of error between calculated flow rate and measured flow rate.

III. Experimental Results and Discussion

NPI characteristics were analyzed for 15 liquids with properties spanning five different conductivities and three viscosities. Fig. 4 presents the results of the Weber number (flow rate) as a function of dimensionless time for six of the liquids with conductivity values ($K \in \{2,10\}$) across all viscosities ($\mu \in \{40,60,80\}$). As seen in Fig. 4, the critical voltage required for a fully continuous jet can be observed across many of the liquids. As expected, the overall flow rate is proportional to the applied voltage. The results in Fig. 4e indicate that for many of the subcritical voltages, the flow rate decays exponentially over time. The jet breakup is indicated by a sharp drop in the flow rate at the end of the sampling period. In correspondence with the findings by [10], the duration of the jet prior to breakup is proportional to the applied voltage. The presence of a dynamic flow rate can likely be attributed to an imbalance between the charges generated within the Taylor cone and those expelled to the substrate. It appears that a greater conductivity aggravates this imbalance, leading to a negative net charge generation within the Taylor cone across a wider range of voltages. Note that the continuous jet regime was not achieved for two of the high conductivity liquids. Examining Figs. Figs. 4d, 4e, and 4f indicate that an increasing viscosity leads to a wider variety of decay constants, while a lower viscosity (Fig. 4d) promotes more consistent decay behavior and initial flow rates.

As expected, the continuous jet regime is generally characterized by a relatively steady flow rate. Two exceptions to this trend appear in Fig. 4b and 4e, as significant changes in the Weber number are observed for an applied voltage of 1050 V and 1200 V, respectively. This observation emphasizes the importance of in situ flow rate sensing, as material properties have been shown to affect the flow rate decay behavior of the continuous jet (CJ) mode. Further, a lower conductivity seems to promote more stable behavior, as the CJ mode is hastily attained upon gradual voltage increments. As seen in Fig. 4a and 4c, once the CJ mode is reached, higher voltages provide a significant boost to the average flow rate of the system. While the flow rate appears to slightly decay following jet impingement, constant flow rate is attained after only a few milliseconds.

While the flow rate model provides a Weber number approximation by measuring the height of the continuous stream, it is only deemed valid under a steady control volume condition (Section II-E). In reality, the system exhibits initial transient behavior for the first few milliseconds across all experiments. This behavior can be seen by plotting the height of the initial deposition as a function of time, shown in Fig. 5. An initial sharp peak can be observed for both the NPI and continuous jet trials followed by an undershoot. In agreement with Fig. 4, the continuous jet regime generally provides a consistent stream height, resulting in a steady flow rate. Furthermore, the NPI regime induces a linearly decreasing stream height leading up to jet breakup. Therefore, the underlying principle for NPI is an insufficient flow rate of

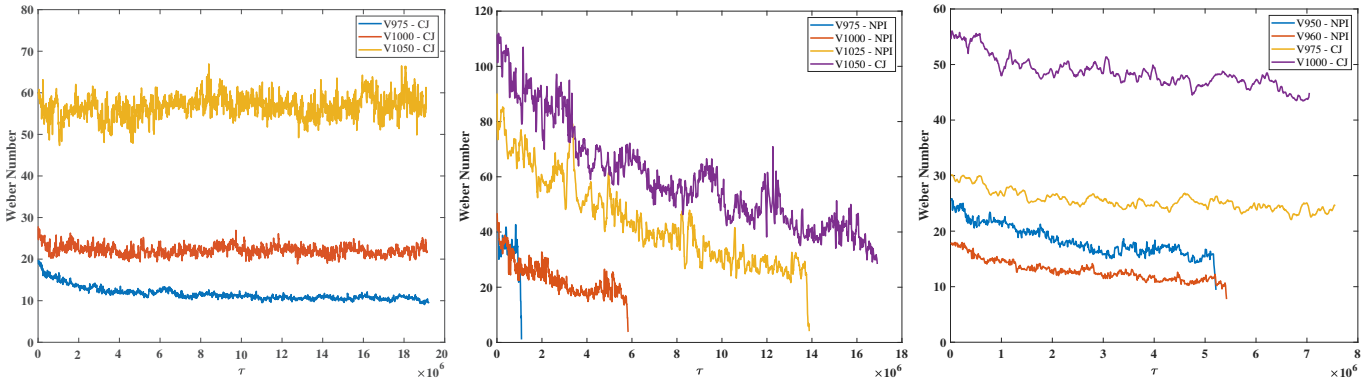

(a) (40,2) (b) (60,2) (c) (80,2)

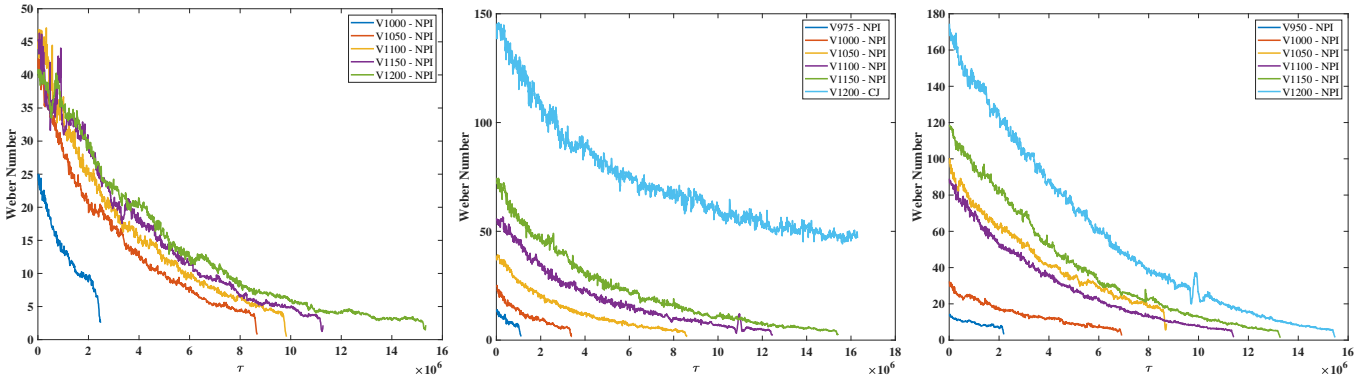

(d) (40,10) (e) (60,10) (f) (80,10)

Fig. 4: Plots depicting Weber number vs. dimensionless time across different liquids (μ [mPa·s],K[μS/cm]).

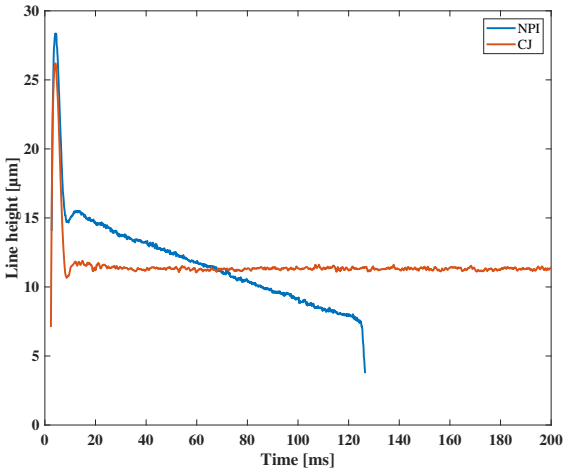

Fig. 6: Height of the printed line at the CV boundary vs. time for NPI and CJ modes.

ink exerted to the substrate. With a constant applied input, the system has been shown to transition out of a desired printing mode. From a controls approach, this behavior can be described as a system instability.

Fig. 5 implies that both regimes can be modeled as a step response of a second order linear system. The initial sharp peak observed in both the NPI and CJ trials is analogous to traditional dynamic friction models, in which the pre-sliding friction induces hysteresis in the response. In e-jet printing, the accumulation of charge in the Taylor cone prior to ejection leads to hysteretic behavior, which manifests as a brief surge of flow rate upon initial impingement.

It is evident that both viscosity and conductivity play key roles in influencing NPI. Therefore, identifying a favorable combination of material properties is essential for attaining stable e-jet behavior. Fig. 7a demarcates the limits of NPI by plotting the initial continuous jet as a function of voltage and material properties, with dashed curves representing approximate continuous boundaries. Fig. 7b provides a more generalized schematic depicting these boundary relationships. Additional regimes are included to broaden the analysis. Hence, it can be assumed that reducing the applied voltage from this boundary results in NPI or no jetting, while applying a greater voltage maintains the continuous jet regime until unstable arcing or multi-jet modes transpire. Fig. 7a highlights the effect of viscosity on the occurrence of NPI, and it can be observed that more viscous liquids reduce the range of stable conductivities. Specifically, continuous jet behavior was not observed for conductivities greater than 4 $\mu S/cm$ for inks on the upper limit of viscosity. In contrast, inks with viscosities of [40,60] mPa·s were found to promote CJ behavior across four of the five experimental conductivities, and the span of voltages required for initial

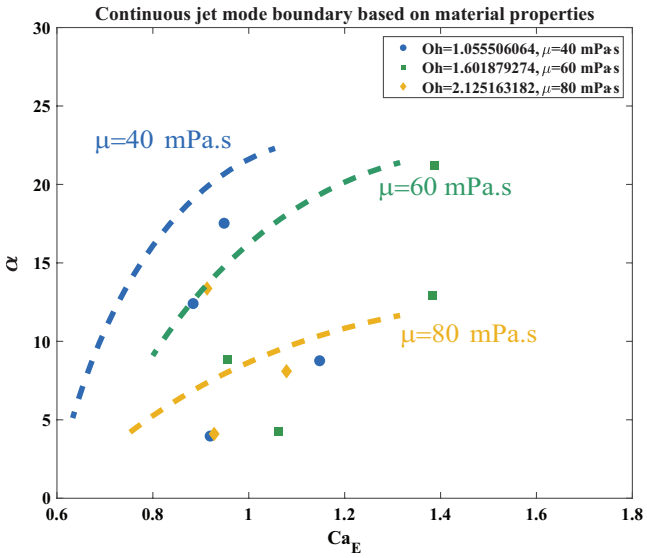

(a)

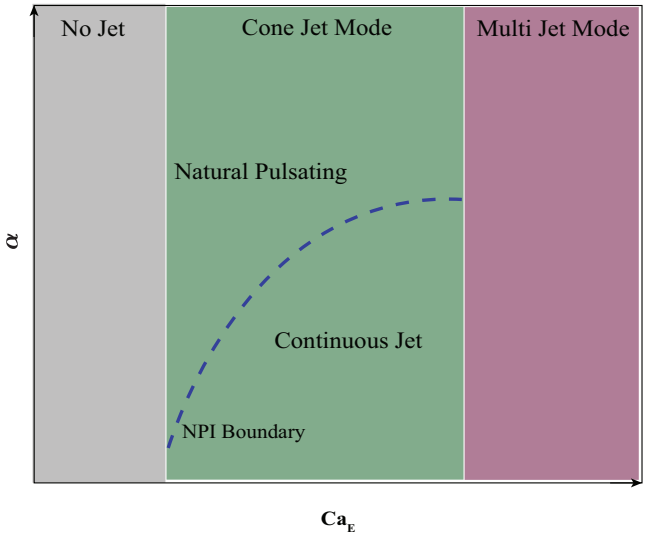

(b)

Fig. 7: (a) Natural Pulsation Initiation (NPI) boundary in α vs. Ca_E graph for different viscosities. (b) Schematic figure of Continuous jet mode vs. Natural Pulsation mode in α vs. Ca_E.

CJ behavior appears to increase with these two viscosity values. In summary, as viscosity increases, it assumes greater importance to limit the material's conductivity in order to maintain a wide space of stable printing inputs.

Considering electronics as a major application of e-jet printing, there exists a need to investigate additional material properties that counter the instabilities associated with high conductivity inks. Future work should analyze NPI across a wider range of conductivities to compare these observed trends.

IV. Conclusion

E-jet printing is a promising additive manufacturing technique with many advantageous properties. While its various printing regimes have been identified and characterized, the transitional behavior from the continuous jet to natural pulsating mode (NPI) is not well understood, and it serves as a barrier for maintain printing stability. This paper uses dimensionless parameters derived from fundamental EHD equations to monitor the ink flow rate during NPI across 15 liquids with varying viscosities and conductivities. A flow rate approximation was implemented to measure the Weber number as a function of time. In contrast with the steady continuous jet mode, NPI exhibited a decaying flow rate over time leading up to jet breakup. A higher conductivity was observed to exacerbate the charge imbalance that instigates NPI. Viscosity appeared to influence the decay rate of the ink flow, as lower values exhibited more consistent decaying behavior.

While the results indicate potential trends in the transitional behavior, future work should consider a wider range of material properties to validate these findings. Considering the applicability of e-jet in printed electronics, additional ink properties can be analyzed to determine their effect on NPI, particularly to counter the unstable behavior associated with conductivity. Finally, future analysis should conduct an in-depth empirical assessment on flow rate decay. This work would support the development of smart in situ flow rate monitoring, which is useful for detecting the onset of potential instabilities.

Appendix I
Further Details on Flow Rate Approximation

As detailed in section II-E, the flow rate model uses two key assumptions to develop a direct relationship between the height of the continuous line and the Weber number of the ink flow as a function of time. Model validation was attained by assessing the agreement of this model's output with the ellipsoidal cap model, presented in Eq. 3. As seen in Fig. 8, the model was configured to report an approximation for the flow rate as a function of time. Curve fitting was implemented with MATLAB to obtain a representative continuous function. Due to the subtle oscillatory nature of the data, a Fourier series containing eight terms was selected as the best fitting model. Integrating the function over the plotted temporal bounds provides an estimate of the total deposited volume throughout NPI.

This volume approximation was then compared with the output of the ellipsoidal cap formula. Metrics for Eq. 3 were obtained using a digital microscope to measure the dimensions of the spheroidal droplet. Model error is reported in Table I.

Appendix II
Droplet Dimensional Proportionality Constant Validation

Assumption 2 in Section II-E states that the ratio of a droplet's height to its base diameter is retained across volumes of similar scale. To validate this assumption, droplets of each liquid were printed and their dimensions were measured using a digital microscope. Fig. 9 displays the

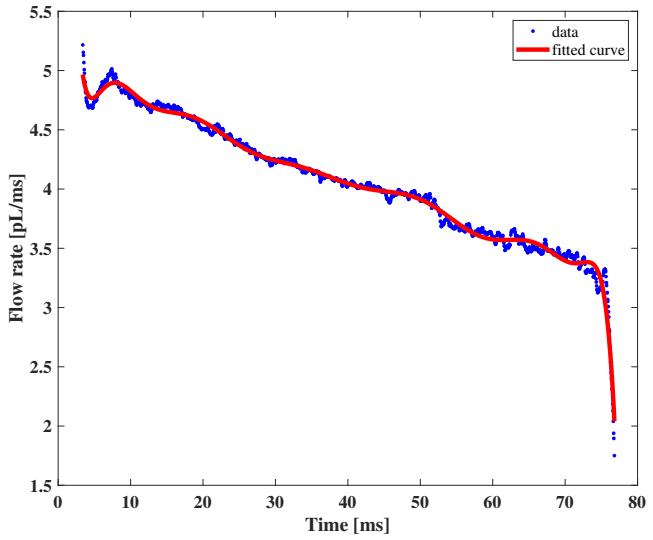

Fig. 8: Fitted curve for flowrate vs. time using an eight-term Fourier series.

results for four of the liquids containing variable viscosities and conductivities. The results of this analysis conclude that this assumption is valid for each liquid individually but not across all of the different liquids. Therefore, the unique ratio for each liquid was inputted into the flow rate model.

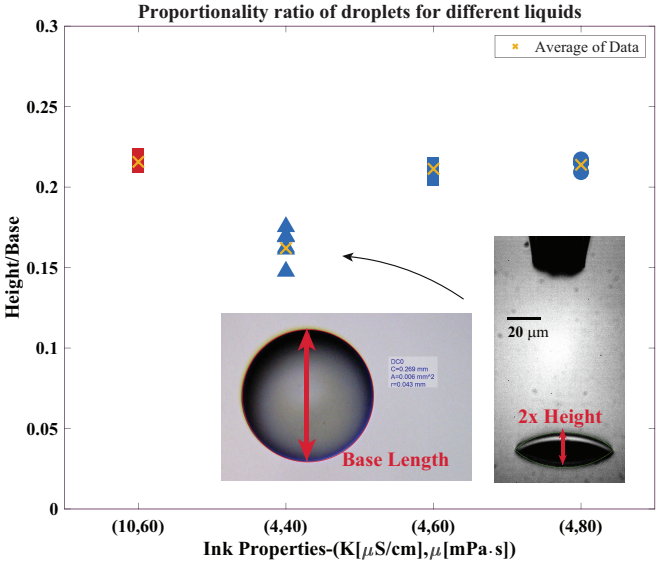

Fig. 9: Height to base ratio of droplets of different liquids. $K = 4\mu$S/cm: (▲:μ = 40mPa·s, ■:μ = 60mPa·s, ●: μ = 80mPa·s); $K = 10\mu$S/cm: (■μ = 60mPa·s); Average:(×).

Appendix III
Ink Properties

Table II provides the composition and relevant material properties of the 15 experimental liquids.

Composition (Glycerine [mL] + DI Water [mL] + NaCl Solution [mL])	μ [mPa·s]	K [μS/cm]	ρ [kg/m^3]	γ [mN/m]
10 + 3.95 + 0.05	40	2	1194.3	65
10 + 3.91 + 0.09	40	4	1194.3	65
10 + 3.86 + 0.14	40	6	1194.3	65
10 + 3.82 + 0.18	40	8	1194.3	65
10 + 3.78 + 0.22	40	10	1194.3	65
10 + 2.92 + 0.08	60	2	1208.4	64.5
10 + 2.85 + 0.15	60	4	1208.4	64.5
10 + 2.79 + 0.21	60	6	1208.5	64.5
10 + 2.72 + 0.28	60	8	1208.4	64.5
10 + 2.65 + 0.35	60	10	1208.4	64.5
10 + 2.41 + 0.09	80	2	1219.5	64.2
10 + 2.32 + 0.18	80	4	1219.5	64.2
10 + 2.22 + 0.28	80	6	1219.5	64.2
10 + 2.14 + 0.36	80	8	1219.5	64.2
10 + 2.06 + 0.44	80	10	1219.5	64.2

TABLE II: Properties of the inks [15]

References

[1] Suresh Kumar Garlapati et al. "Printed Electronics Based on Inorganic Semiconductors: From Processes and Materials to Devices". In: *Advanced Materials* 30.40 (2018), p. 1707600. DOI: https://doi.org/10.1002/adma.201707600. eprint: https://onlinelibrary.wiley.com/doi/pdf/10.1002/adma.201707600. URL: https://onlinelibrary.wiley.com/doi/abs/10.1002/adma.201707600.

[2] Sihang Ma et al. "Ultra-Thin Chips with Printed Interconnects on Flexible Foils". In: *Advanced Electronic Materials* 8.5 (2022), p. 2101029. DOI: https://doi.org/10.1002/aelm.202101029. eprint: https://onlinelibrary.wiley.com/doi/pdf/10.1002/aelm.202101029. URL: https://onlinelibrary.wiley.com/doi/abs/10.1002/aelm.202101029.

[3] Kuipeng Zhao et al. "Drop-on-Demand Electrohydrodynamic Jet Printing of Graphene and Its Composite Microelectrode for High Performance Electrochemical Sensing". In: *Journal of the Electrochemical Society* 167.10, 107508 (Jan. 2020), p. 107508. DOI: 10.1149/1945-7111/ab9c7e.

[4] Jang-Ung Park et al. "Nanoscale Patterns of Oligonucleotides Formed by Electrohydrodynamic Jet Printing with Applications in Biosensing and Nanomaterials Assembly". In: *Nano Letters* 8.12 (Oct. 2008). DOI: 10.1021/nl801832v.

[5] Erick Sutanto et al. "Electrohydrodynamic jet printing of micro-optical devices". In: *Manufacturing Letters* 2.1 (2014), pp. 4–7. ISSN: 2213-8463. DOI: https://doi.org/10.1016/j.mfglet.2013.10.007. URL:

https://www.sciencedirect.com/science/article/pii/S2213846313000242.

[6] Zahra Afkhami et al. "Electrohydrodynamic Jet Printing of One-Dimensional Photonic Crystals: Part I—An Empirical Model for Multi-Material Multi-Layer Fabrication". In: *Advanced Materials Technologies* 5.10 (2020), p. 2000386.

[7] S Mishra et al. "High-speed and drop-on-demand printing with a pulsed electrohydrodynamic jet". In: *Journal of Micromechanics and Microengineering* 20.9 (Aug. 2010), p. 095026. DOI: 10.1088/0960-1317/20/9/095026. URL: https://dx.doi.org/10.1088/0960-1317/20/9/095026.

[8] Reinhard Juraschek and Franz W. Röllgen. "Pulsation phenomena during electrospray ionization". In: *International Journal of Mass Spectrometry* 177 (1998), pp. 1–15.

[9] Ayodya Tenggara et al. "High Aspect Ratio Conductive Lines Fabricated by Electrohydrodynamic (EHD) Jet Printing". In: Nov. 2014.

[10] Angelo Hawa, Ali Bahrami, and Kira Barton. "The Effect of Voltage on The Initiation of Natural Pulsation in Electrohydrodynamic Jet Printing". In: (2023). DOI: https://doi.org/10.31224/2820.

[11] R. Juraschek and F.W. Röllgen. "Pulsation phenomena during electrospray ionization". In: *International Journal of Mass Spectrometry* 177.1 (1998), pp. 1–15. ISSN: 1387-3806. DOI: https://doi.org/10.1016/S1387-3806(98)14025-3. URL: https://www.sciencedirect.com/science/article/pii/S1387380698140253.

[12] Robert T. Collins et al. "Universal scaling laws for the disintegration of electrified drops". In: *Proceedings of the National Academy of Sciences* 110.13 (2013), pp. 4905–4910. DOI: 10.1073/pnas.1213708110. URL: https://www.pnas.org/doi/abs/10.1073/pnas.1213708110.

[13] C.-H. Chen, D. A. Saville, and I. A. Aksay. "Scaling laws for pulsed electrohydrodynamic drop formation". In: *Applied Physics Letters* 89.12 (2006), p. 124103. DOI: 10.1063/1.2356891. eprint: https://doi.org/10.1063/1.2356891. URL: https://doi.org/10.1063/1.2356891.

[14] Hong Kyoon Choi et al. "Scaling laws for jet pulsations associated with high-resolution electrohydrodynamic printing". In: *Applied Physics Letters* 92.12 (2008), p. 123109. DOI: 10.1063/1.2903700. eprint: https://doi.org/10.1063/1.2903700. URL: https://doi.org/10.1063/1.2903700.

[15] Lei Guo et al. "Experimental Study of the Influence of Ink Properties and Process Parameters on Ejection Volume in Electrohydrodynamic Jet Printing". In: *Micromachines* 9 (Oct. 2018), p. 522. DOI: 10.3390/mi9100522.

[16] A. J. Hijano et al. "Periodic emission of droplets from an oscillating electrified meniscus of a low-viscosity, highly conductive liquid". In: *Phys. Rev. E* 91 (1 Jan. 2015), p. 013011. DOI: 10.1103/PhysRevE.91.013011. URL: https://link.aps.org/doi/10.1103/PhysRevE.91.013011.

[17] D. A. Saville. "ELECTROHYDRODYNAMICS: The Taylor-Melcher Leaky Dielectric Model". In: *Annual Review of Fluid Mechanics* 29.1 (1997), pp. 27–64. DOI: 10.1146/annurev.fluid.29.1.27.

[18] JR Melcher and GI Taylor. "Electrohydrodynamics: a review of the role of interfacial shear stresses". In: *Annual review of fluid mechanics* 1.1 (1969), pp. 111–146.

[19] Qichun Nie et al. "Designing working diagrams for electrohydrodynamic printing". In: *Chemical Engineering Science* 240 (2021), p. 116661.

[20] Frank M. White. *Fluid mechanics*. 6th ed. Mcgraw-Hill series in mechanical engineering. New York, NY: McGraw-Hill, 2009. ISBN: 978-0-07-352934-9.

[21] Jonathan Stringer and Brian Derby. "Formation and stability of lines produced by inkjet printing". In: *Langmuir* 26.12 (2010), pp. 10365–10372.

[22] Paul C Duineveld. "The stability of ink-jet printed lines of liquid with zero receding contact angle on a homogeneous substrate". In: *Journal of Fluid Mechanics* 477 (2003), pp. 175–200.

[23] *Circular Segment Kernel Description*. https://mathworld.wolfram.com/CircularSegment.html.